Journal of Materials Chemistry A

PAPER

View Article Online
View Journal | View Issue

Cite this: J. Mater. Chem. A, 2015, 3, 12680

Suspension plasma sprayed coatings using dilute hydrothermally produced titania feedstocks for photocatalytic applications†

B. W. Robinson,*[a] C. J. Tighe,[a] R. I. Gruar,[a] A. Mills,[b] I. P. Parkin,[a] A. K. Tabecki,[c] H. L. de Villiers Lovelock[c] and J. A. Darr[a]

Received 9th October 2014
Accepted 20th April 2015

DOI: 10.1039/c4ta05397d

www.rsc.org/MaterialsA

Titanium dioxide coatings have potential applications including photocatalysts for solar assisted hydrogen production, solar water disinfection and self-cleaning windows. Herein, we report the use of suspension plasma spraying (SPS) for the deposition of conformal titanium dioxide coatings. The process utilises a nanoparticle slurry of TiO_2 (*ca.* 6 and 12 nm respectively) in water, which is fed into a high temperature plasma jet (*ca.* 7000–20 000 K). This facilitated the deposition of adherent coatings of nanostructured titanium dioxide with predominantly anatase crystal structure. In this study, suspensions of nano-titanium dioxide, made *via* continuous hydrothermal flow synthesis (CHFS), were used directly as a feedstock for the SPS process. Coatings were produced by varying the feedstock crystallite size, spray distance and plasma conditions. The coatings produced exhibited *ca.* 90–100% anatase phase content with the remainder being rutile (demonstrated by XRD). Phase distribution was homogenous throughout the coatings as determined by micro-Raman spectroscopy. The coatings had a granular surface, with a high specific surface area and consisted of densely packed agglomerates interspersed with some melted material. All of the coatings were shown to be photoactive by means of a sacrificial hydrogen evolution test under UV radiation and compared favourably with reported values for CVD coatings and compressed discs of P25.

1. Introduction

Titania (titanium dioxide, TiO_2) under atmospheric pressure exists as amorphous, anatase, brookite and rutile forms, however, the vast majority of research in solar driven applications focuses on anatase and rutile due to their stability and marked photoactivity.[1–3] These materials have been shown to have applications in photo-driven water/air purification and energy harvesting devices, for example through a photolysis device.[4,5] These applications are photo-driven processes that rely on photoexcitation events initiated by absorption of incident light of appropriate wavelength. Due to the band gap of anatase (*ca.* 3.2 eV), this form of titania typically absorbs in the UV portion of the solar spectrum ($\lambda < 387$ nm), although this can be altered with doping or the use of a sensitizer material or molecule.[6–8] There have been many attempts to fabricate photoactive titania coatings *via* techniques including chemical vapour deposition (CVD), dip coating, screen printing and thermal spraying.[9–15]

In conventional thermal spraying a powder is usually fed from a hopper into the plasma or flame apparatus *via* a carrier gas, whereby the powder is then melted in flight and impacts on to a substrate. Feeding powders in this way has inherent problems as all powders have to be carefully selected to have the right flow properties so that they can be fed without blockages, which requires additional effort (sieving) and limits the range of usable particle sizes.[16] Using suspension thermal spraying, high quality coatings have reportedly been achieved by the use of commercial titanium dioxide nanopowder suspensions rather than a dry thermal spray powder feed, *via* suspension plasma spraying (SPS).[17–19] In this process, a suspension of titania is fed into a plasma jet, which evaporates the liquid causing the material to agglomerate, and can melt the particles while accelerating them onto a substrate where they impact to form a coating. This technique can yield high anatase content (>80%) nanostructured coatings with significant photocatalytic activity, which is unachievable *via* traditional thermal spray processes *e.g.* high velocity oxy-fuel spray.[14,20]

A significant challenge in SPS is the formation of an initial stable suspension of the titanium dioxide, which is essential to facilitate uniform delivery of the feedstock. Unstable suspensions undergo agglomeration and settling, which can result in

[a]Department of Chemistry, University College London, 20 Gordon Street, London, WC1H 0AJ, UK. E-mail: zccad78@live.ucl.ac.uk

[b]School of Chemistry and Chemical Engineering, Queen's University Belfast, David Keir Building, Belfast BT9 5AG, UK

[c]TWI Ltd., Granta Park, Cambridge, CB21 6AL, UK

† Electronic supplementary information (ESI) available. See DOI: 10.1039/c4ta05397d

blockage of lines and injectors.[16] Suspension spray is a relatively new technology and commercially available suspensions are sparse. Typically, published work on suspension spray of titania, whether *via* high velocity suspension flame spraying (HVSFS) or SPS, has been conducted using suspensions of *ca.* 10–25 wt%, with a primary crystallite size typically in the range 5–25 nm.[20–25]

Herein, we report the first use of a nanoparticle suspension made *via* continuous hydrothermal flow synthesis (CHFS) in an SPS technique for the production of adherent TiO_2 conformal coatings. CHFS has the benefit of producing nanoparticles of selectable size and composition with the end product collected as an aqueous dispersion. This negates the need for dispersion of commercial nanopowder and minimises exposure to free nanoparticles in dry powder form, a noted health concern. Suspensions of *ca.* 5 wt% were used as it resulted in a readily re-dispersible semi-stable suspension. The increased amount of water in the suspension was also presumed to absorb additional energy from the plasma, in order to retain a greater amount of the anatase phase and feedstock nanostructure in the coating. Using a dilute system also slows down the coating build up greatly, allowing thin coatings to be made. This aspect is of particular importance in photocatalytic applications, as for thin coatings, photo-generated electrons and holes have a shorter distance to travel before they reach the surface for reaction and are less likely to recombine, increasing photocatalytic activity.[26] The cleaned suspensions produced from CHFS contain only nano-titania and deionised water; no additional stabilisers were used to keep the titania in suspension. Furthermore, a benefit of CHFS is that it uses water as both the reagent and a green solvent. This is important to reduce the environmental footprint and avoid the use of toxic organic solvents which can be wasteful and environmentally unfriendly.[27] The CHFS process is also very scalable up to tonnes per year. The authors have developed a pilot plant CHFS reactor which is capable of producing *ca.* 3 TPA.[28,29]

2. Experimental procedure

2.1. Feedstock materials

Nano-titania (12 and 6 nm primary crystallite size) suspensions were synthesised using a continuous hydrothermal flow synthesis pilot plant located at UCL (Fig. 1); the details of the pilot plant and mixer used for the process are described in detail elsewhere.[27,30,31] Briefly, in CHFS a stream of supercritical water is brought into contact with a stream of metal salts at ambient temperature leading to nucleation of metal oxide nanoparticles *via* instantaneous hydrolysis and dehydration reactions. The reaction was facilitated by the development of a patented confined jet-mixer which controls the mixing of reactants and nucleation of nanoparticles, without blockage of the reactor (Table 1).[27]

The following overall reaction applies to the reaction of the precursor in the presence of base and supercritical water:

$$TiOSO_4 + mKOH + (1 - m)H_2O \rightarrow TiO_2 + (m/2)K_2SO_4 + (1 - m/2)H_2SO_4$$

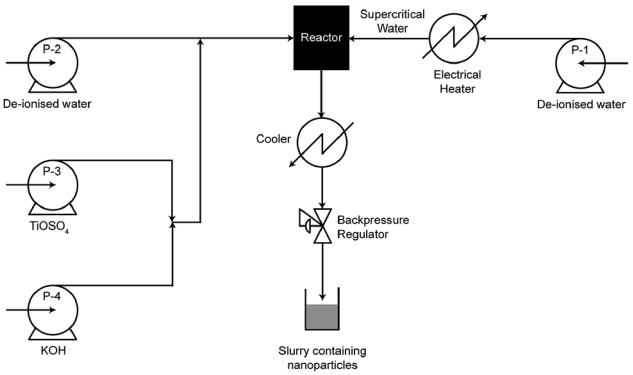

Fig. 1 Schematic of the CHFS pilot plant configured for the production of 6 nm titania suspensions.

Table 1 Parameters of titania feedstock synthesis

	Concentration/ mol dm^{-3}		Flow rate/mL min^{-1}	
Precursor	6 nm	12 nm	6 nm	12 nm
$TiOSO_4$	1.0	1.0	185	200
KOH	2.0	2.35	185	119
DI water feed 1	—	—	400	400
DI water feed 2	—	—	30	81

The slurries that were collected from the CHFS pilot plant were made as a *ca.* 1 wt% milky suspension. The suspension was concentrated by the addition of sodium chloride until separation and transferred to a dialysis tube to clean the supernatant. The suspension was concentrated by centrifugation to *ca.* 25 wt% and stored until required. Prior to spraying, the concentrated suspension was diluted with deionized water to give *ca.* 5 wt% white titania suspension.

2.2. Suspension spraying

SPS was performed using a Praxair®SG-100 torch mounted on a OTC AII-V20 robot (Fig. 2A) which had been modified to incorporate a suspension spray nebuliser which facilitated the addition of the slurry to the plasma torch. The nanoparticle suspension was fed to the external nebuliser (constructed from a modified RS air brush AB931) using an ISCO® 260D syringe pump set at a flow rate 5 mL min^{-1} (Fig. 2B). All coatings were plasma sprayed onto 25 × 25 × 0.5 mm AISI 304 stainless steel plates which had been ferric acid etched for a period of *ca.* 30 seconds. The substrates were water cooled throughout spraying (using a customised heat exchange system attached to the back face of the substrate) to prevent overheating and consequent distortion of the thin steel substrate (Fig. 2B). While spraying the samples associated with the 6 nm Ar/H_2 65 mm spray distance conditions, a partial blockage occurred which led to a marked effect on the coating properties, as discussed below (Table 2).

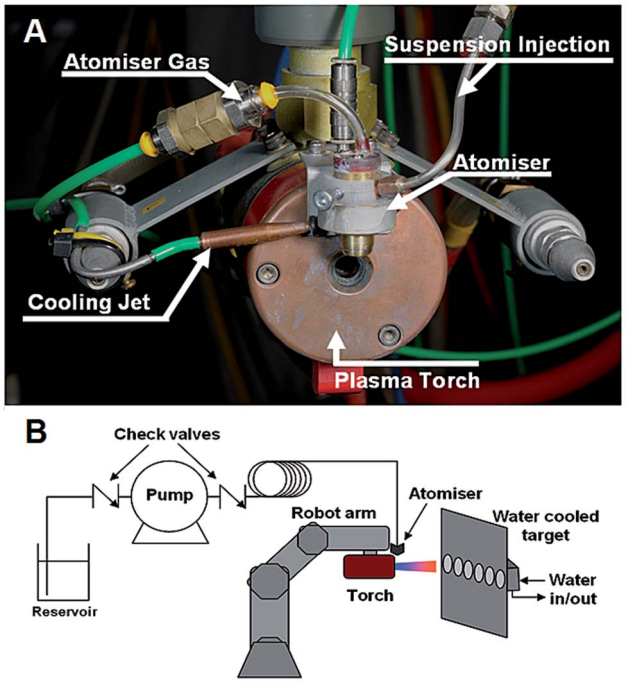

Fig. 2 Suspension plasma spray set-up with attached cooling and suspension injection systems (A). Schematic of the apparatus used for SPS of nano-titania suspension in water (B).

Table 2 SPS parameters

	Parameter sets	
Spray parameter	Ar/H_2	Ar
Ar plasma gas flow rate/L min^{-1}	49	49
H_2 plasma gas flow rate/L min^{-1}	0.9	—
Plasma voltage/V	45	25
Plasma current/A	700	450
Argon atomisation gas flow rate/L min^{-1}	3	3
Number of spray passes	10	10
Spray distance/mm	55–85	55–85
Cooling water temperature/°C	55	55

2.3. Coating characterisation

The coated samples were analysed using a Bruker AXS D8 (GADDS) diffractometer using a Cu K-Alpha X-ray source (λ = 0.154 nm). From the X-ray powder diffraction data, the phase composition was calculated by integrating and comparing the anatase (101) and rutile (110) peaks (eqn (1)).

$$C_A = 8I_A/[8I_A + 13I_R] \quad (1)$$

where I_A and I_R are the anatase (101) and rutile (110) relative peak intensities.[19] Furthermore, the Scherrer equation was used to estimate crystal size (eqn (2))

$$t = K\lambda/B\cos\theta \quad (2)$$

where λ is the X-ray wavelength, θ is the Bragg diffraction angle in degrees, B is the full width half maximum (in radians) and K is the shape factor, in this case 0.9.

The mass of the coatings was determined by pre-weighing each substrate using a Sartorius CPA four-figure Analytical Balance CPA324S. Coated substrates were subsequently weighed with the difference assumed to be the coated mass.

SEM analysis was performed using a LEO 1550 Field Emission Scanning Electron Microscope (FESEM). EDX analysis was performed using an EDAX spectrometer with Pegasus software.

Micro-Raman spectroscopy was performed using a Renishaw inVia Raman microscope, measuring in the wavenumber range 100 to 1000 cm^{-1}.

UV-Vis spectroscopy was performed using a Lambda 950 UV/Vis/NIR spectrophotometer in reflectance mode between 200 and 1500 nm.

For the photocatalysis hydrogen production tests, the backs of the coated steel plates were sputter coated with platinum. The photoactivity of the coating was measured by observing the rate of hydrogen production in a sacrificial solution of 0.1 M HCl in ethanol and water (1 : 1). The coatings were irradiated with two 8 W 365 nm UV lamps at a distance of 10 cm. The UV irradiance of the lamps at this distance was *ca.* 2 mW cm^{-2}. The gas produced was analysed in a Varian CP-3800 Gas Chromatograph every 15 minutes for a total of 120 minutes to determine hydrogen production rate.[32–34]

For cross-sectional SEM imaging, samples were mounted by vacuum impregnating them with epoxy resin containing conductive filler, and then sectioned using a precision saw (Brilliant 220) and ground anti-clockwise using a series of SiC papers (P120, P320, P600, P1200 and P2500 sia Abrasives Brighouse, UK) at a speed of 300 rpm. The specimens were then polished with a 3 μm and 1 μm cloth at a speed of 500 rpm.

3. Results and discussion

3.1. Visual examination of the coatings

Coatings produced using the pure Ar plasma were light grey in colour while those produced using an Ar/H_2 plasma varied with spray distance from dark grey/blue at the shortest distance to light grey at the furthest (Fig. 3). This change from the

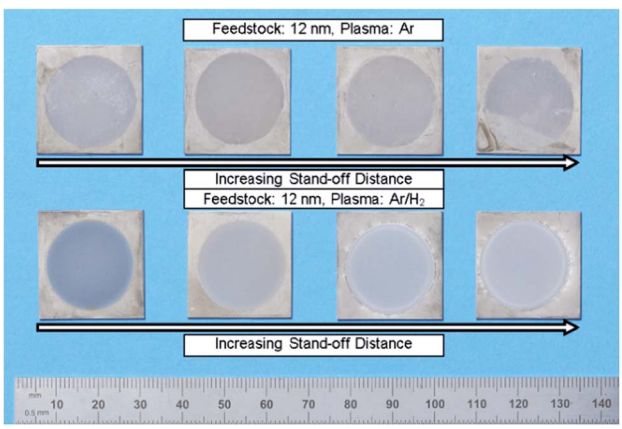

Fig. 3 Photograph showing 12 nm titania feedstock coatings produced by SPS in Ar and Ar/H_2 plasma conditions at the range of stand-off distances. Coatings are produced as circles due to their mounting in the water cooled jig.

suspensions' initial white colour during processing indicates the formation of Ti^{3+} in the coatings.

3.2. Coating thickness and mass

Thickness was measured by SEM imaging of coating cross-sections (Fig. 10). Coating thicknesses were in the range 2–15 μm, with coating masses of 4–10 mg per stub (equating to a loading of 1.1–2.5 mg cm^{-1}), varying with spray distance. The low thickness observed for these coatings demonstrates the possibility of producing thin coatings closer to the realm of CVD/PVD by suspension spray. This thickness control is enhanced by the use of the low concentration suspension.

3.3. Phase composition

Titania has three common crystalline phases anatase, brookite and rutile at atmospheric pressure. Both the anatase and brookite phases are metastable converting to rutile upon heating, with anatase transforming in the range 400–1200 °C, depending on a number of factors including crystal size and impurities.[35] It has been shown that phase composition can have a significant effect on the activity of a titania coating, with some commercial materials possessing *ca.* 80% anatase and 20% rutile.[36] This enhanced activity is believed to be due to a synergic interaction between the two phases.[37] Rutile has a smaller band gap (3.0 eV relative to 3.2 eV for anatase) so therefore absorbs more of the available energy, however, due to an increased electron–hole recombination rate relative to the anatase phase, it is presumed to be less active. A mixture of phases can offer a balance to give an enhanced overall photoactivity. Also, the conduction band positioning of the two phases is such that when in contact, electrons will flow from the anatase to the rutile, and holes *vice versa*, therefore allowing vectorial charge separation. However, the direction of charge carrier motion is still disputed.[38]

Phase composition of the SPS coatings as a function of spray distance and plasma type is shown in Fig. 4. For coatings deposited using a Ar/H_2 plasma, there is a general trend of increasing anatase content with increasing spray distance. In contrast, coatings deposited using an Ar plasma were essentially pure anatase, except for short stand-off distances of 55 mm, where some rutile was observed. For coatings produced using 12 nm titania in an Ar/H_2 plasma, anatase phase content rose from *ca.* 92% to *ca.* 98% as spray distance increases from 55 to 85 mm. For the coatings produced using 6 nm titania in an Ar/H_2 plasma, the anatase phase rose almost linearly from *ca.* 90% to *ca.* 100% with spray distance in the range 55 to 85 mm.

These results can be understood in terms of the resolidification pathway of the molten titania particles. It has been found that spray distance can have a significant effect on the phase composition of the coating by altering the resolidification pathway.[17] Due to the high enthalpy of the plasma, the water in the suspension quickly evaporates and many of the particles melt. Once molten, the material can either resolidify on the substrate or in flight (or a mixture of the two) depending on the spray parameters used. Agglomerates resolidifying in flight undergo homogeneous nucleation which causes anatase to

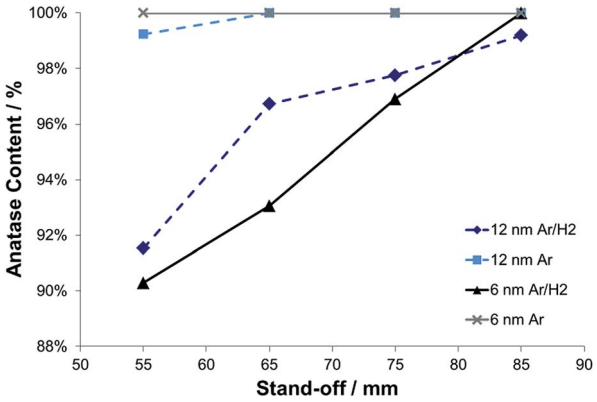

Fig. 4 The effect of spray distance on coating phase composition for the two titania feedstocks and plasmas used.

form due to the decreased interfacial energy for the anatase phase (despite the lower Gibbs free energy of rutile). At longer spray distances there is longer time for resolidification in flight, leading to increasing proportions of anatase phase. This trend appears to be consistent with the results of this study. Agglomerates which solidify on the substrate can form rutile or anatase depending on size. Agglomerates solidifying in contact with the surface can undergo heterogeneous nucleation thus forming rutile phase due to the lower Gibbs free energy for rutile relative to the anatase phase. However if the agglomerates are submicron in size, solidification on the surface can occur fast enough to suppress heterogeneous nucleation in favour of homogeneous nucleation and generate metastable anatase phase.[39] The difference in phase composition between the coatings produced using an Ar plasma and those produced

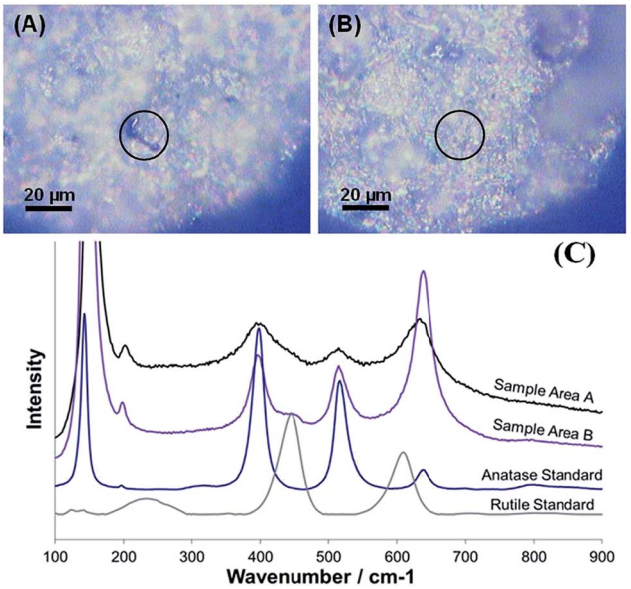

Fig. 5 Raman spectra (c) of two areas (sample area A (a), sample area B (b)) of a titania coating produced in an Ar/H_2 plasma from a 12 nm feedstock, with reference spectra.[41,42] The circles on images A and B correspond to the analysed areas.

using an Ar/H_2 plasma was attributed to a combination of factors. The particles in the Ar plasma reached a lower temperature than those in the Ar/H_2 plasma, due to the lower enthalpy of the plasma, so less of the titania melted (this is supported by the SEM observations, where little melted titania material was observed, Fig. 9). A separate contributing factor may be the lower electrical power relative to the Ar/H_2 system, which resulted in decreased particle velocities (due to the reduced pinch effect which acts to confine the plasma, hence increasing velocity), allowing greater inflight time for resolidification so that practically no rutile was observed in the coating. It is also possible that metastable anatase formed from the molten phase because of the use of water cooling by direct contact with the steel substrate, which gave more efficient cooling than the more commonly used air cooling or uncooled substrates. This would be expected to lead to increased anatase content in all coatings produced. The effect of substrate temperature on phase composition of SPS titania coatings has been previously highlighted by Mauer *et. al.*[40]

As stated earlier, in commercial optimised photocatalysts such as P25, excellent photocatalytic activity can be achieved through control of titania phases in intimate contact and particle size to enhance vectorial charge separation and maximise light absorption. In such cases, the properties rely on the catalyst possessing an intricate mixing of rutile and anatase phases, which allows movement of electrons and holes between the two.[37]

To determine the extent of phase mixing, micro-Raman spectroscopy was used. The analysed results from the micro-Raman spectroscopy were in broad agreement with the XRD data: the spectra collected showed that the coatings were largely composed of anatase. However, micro-Raman did show that coatings produced using the Ar plasma, previously thought to be 100% anatase by XRD, contained trace amounts of rutile. This is visible as a broadening of the B_{1g} peak located at 400 cm^{-1} and the E_g peak located at 640 cm^{-1} indicating the presence of rutile peaks typically found at 447 (E_g) and 612 cm^{-1} (A_{1g}). The remaining peaks: 146 (E_g), 197 (E_g) and 516 (A_{1g}, B_{1g}) all correspond with the anatase phase.

During micro-Raman analysis, small black/blue areas which had a greater proportion of rutile phase than the homogenous surrounding material (typically anatase) were observed (a cluster of three can be seen in Fig. 5a). It is thought that these structures correspond to the deformed and inflight resolidified agglomerates in the coating (Fig. 6). This explains why these areas can be either anatase or rutile, depending on the solidification pathway. These structures were approximately a few microns in size based on SEM analysis, in agreement with observations made during micro-Raman spectroscopy. Coatings produced from Ar/H_2 plasmas contained greater amounts of both the deformed and the inflight resolidified material types, visible in SEM imaging, correlating with a greater number of black/blue areas visible in the coatings during the micro-Raman examination. These structures can be distinguished under SEM by shape. Resolidified material (anatase) appears as fully rounded spheres (Fig. 6-3), deformed surface resolidified material (rutile) appears smooth and spread across the coating surface (Fig. 6-1). Partially molten material (anatase) is characterised by a round shape but with granular structure still visible (Fig. 6-2).

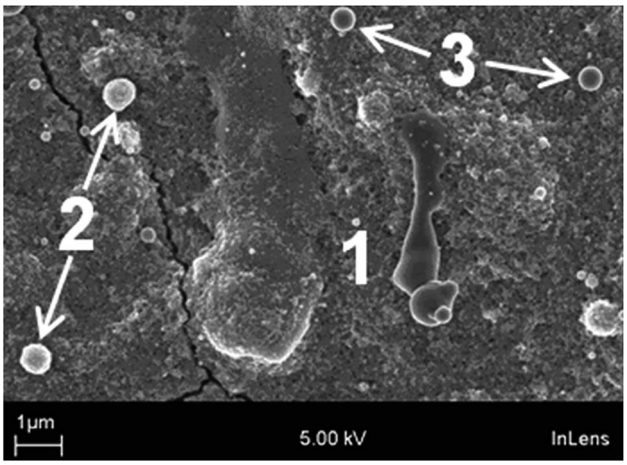

Fig. 6 The microstructure of a titania coating consisting of deformed melted material solidified on the surface (1, rutile), agglomerates which are partially melted (2, anatase) and those which have resolidified in flight (3, anatase).

From micro-Raman analysis it can be said that there is a homogeneous distribution of rutile and anatase, with the rutile being generally localised in small areas of *ca.* 3 μm in size. These areas were visible under the optical microscope (part of area selection in micro-Raman analysis) as black/blue dots/smudges. This is due to an increased concentration of Ti^{3+} due to the greater temperature reached by this material during coating, leading to a loss of oxygen with additional reduction caused by the presence of hydrogen. Areas such as this give the coatings a grey/blue appearance (Fig. 3). These areas were also shown to consist intermittently of anatase phase. However, in these less frequent circumstances, it would seem that these structures are agglomerates that have resolidified in flight; a process which forms anatase material

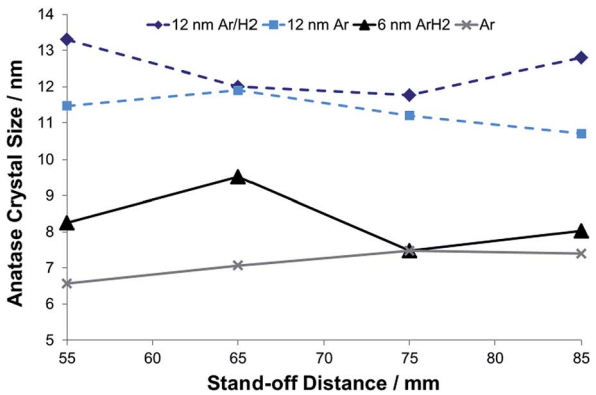

Fig. 7 The effect of spray distance on anatase crystallite size in coatings produced using Ar and Ar/H_2 plasmas using two feedstocks containing 6 and 12 nm titania crystallites. A partial blockage of suspension feed occurred during the coating of the 6 nm Ar/H_2 65 mm stand-off specimens leading to an inconsistent temperature.

(Fig. 6-3) as opposed to the surface-resolidifying rutile titania (Fig. 6-1).

3.4. Crystallite size

Both crystallite size and phase composition are known to have a significant effect on photoactivity. Crystallite size has been shown to influence the size of the bandgap leading to an increase in bandgap with decreasing crystal size. This increased bandgap decreases the percentage of available light that the material can absorb, lowering photoactivity. Recombination rate has also been shown to be affected by crystallite size, altering the rate of surface and bulk recombination independently. Crystallite size also affects surface area, with a smaller crystallite size, surface area increases, increasing access to active sites and therefore photoactivity. So, appropriate selection of crystallite size is important for maximising activity; in some cases a linear relationship of increasing photoactivity has been observed for anatase crystallites in the range 10–32 nm.[43,44] The coatings' anatase crystallite sizes were determined by XRD (by application of the Scherrer equation) with the effect of plasma condition and spray distance considered as summarised in Fig. 7.

The crystallite size of the coatings was assessed from the powder diffraction data by application of the Scherrer equation to the (101) anatase peaks. There appeared to be no significant trend in crystal size with stand-off distance despite the increase in flight time before collision with the substrate (Fig. 7). There was an observable difference between coatings deposited with the two plasma conditions used. The greater enthalpy of the Ar/H_2 plasma led to greater sintering. Coatings produced with the Ar plasma seem to have undergone little or no significant sintering, with the 6 nm feed material staying at *ca.* 6 nm post process. The 12 nm titania coatings had crystallite sizes ranging just under 12 nm after spraying, which is within uncertainties in the application of the Scherrer equation. It is also possible that there may be some micro-strain generated by the presence of reduced titania species, causing line broadening; the presence of these species in plasma sprayed titania coatings has been previously highlighted by Toma *et al.*[21] Typically it would be expected that crystallites would agglomerate and sinter as the solution evaporates and particles heat up, due to the large surface area of the nano-crystals. From this it can be said that the Ar plasma does not heat the particles enough to cause significant sintering of either of the titania materials used. However, this may be due to the sintering particles going on to transform to rutile and therefore being excluded from this measurement. Peak intensity for the rutile phase was too low to determine crystallite size for all coatings by this method. However, rutile crystal size can be estimated to be approximately 40–90 nm. The coatings produced using the higher enthalpy Ar/H_2 plasma have undergone some sintering: coatings produced from the 12 nm titania sintered to *ca.* 13 nm, whereas those produced from the 6 nm titania have grown to *ca.* 8 nm. For the 6 nm Ar/H_2 coating at 65 mm spray distance, a decreased injection rate (caused by an unplanned partial blockage in the feed) led to a relatively "hotter" plasma and more sintering than for the other coatings produced under similar conditions.

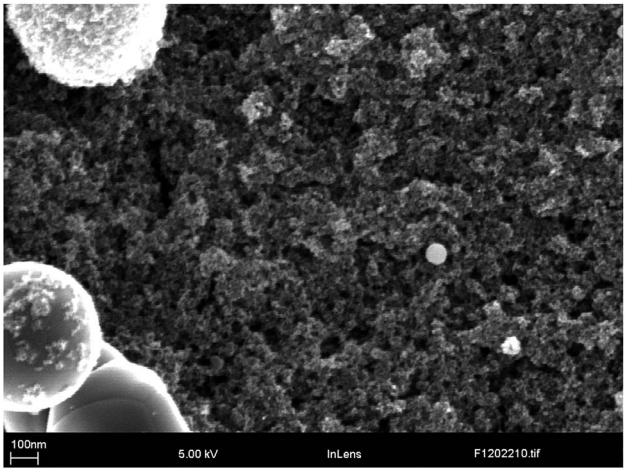

Fig. 8 The surface of a 6 nm coatings produced in a Ar/H_2 plasma with the dense packing of fine agglomerates (*ca.* 50 nm) that make up the majority of the coating. Also visible is a number of small melted agglomerates *ca.* 0.5 μm in size.

3.5. Coating surface structure

All coatings produced were composed of majority granular zones consisting of densely packed agglomerates *ca.* 20–100 nm in size (Fig. 8), similar to that of the feedstocks. These areas give the coatings the large surface area that is desirable for absorption in technologies such as water purification or photolysis devices. A number of larger agglomerates up to approximately ten microns were also visible in the coating.

Coatings produced in Ar/H_2 plasma conditions showed significantly more melted material scattered on the surface (Fig. 9). This was consistent with the observation of increased phased transformation for Ar/H_2 coatings, compared to those produced in Ar plasmas as reported herein and in the literature.[21] This was due to the greater enthalpy of the plasma with the addition of hydrogen. At extended stand-off distances, agglomerates visible in Ar/H_2 coatings appeared more rounded due to resolidification inflight and less deformation on the surface.

There were some cracks visible in the surface of coatings produced from the 6 nm feedstock in both plasma conditions. This suggested a lower adhesive strength of these coatings possibly due to the lower momentum of the 6 nm particles relative to the 12 nm particles. Also visible in the coatings composed of the 12 nm feedstock was a quantity of potassium sulphate (confirmed by XRD and EDX), a residual impurity of the CHFS process due to incomplete dialysis. However this did not appear to affect the coating properties.

3.6. Coating microstructure

SEM analysis was performed on coating cross sections to determine the microstructure. Images showed agreement with surface SEM imaging and XRD results, with coatings produced

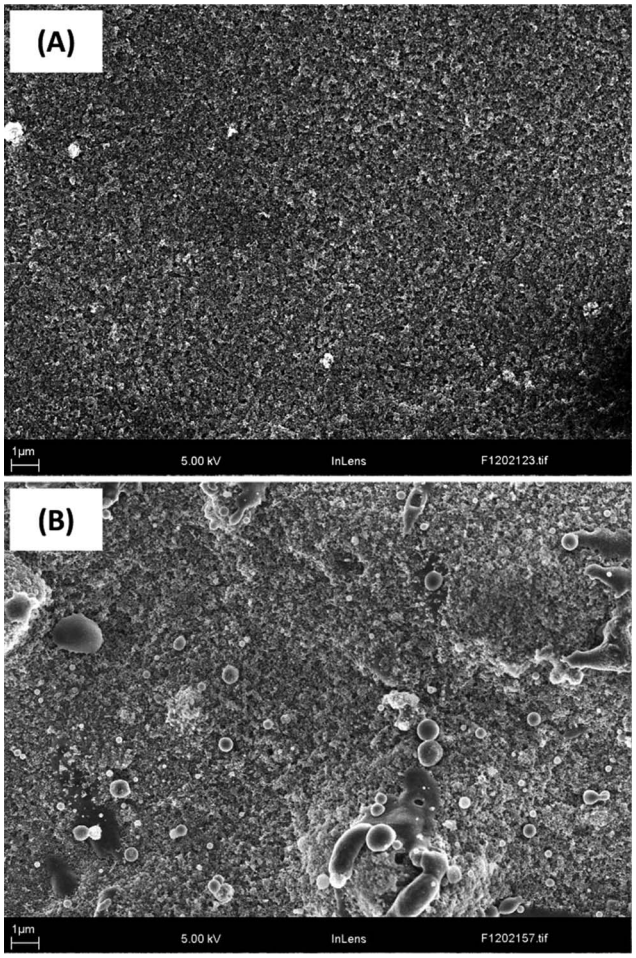

Fig. 9 The surface of 12 nm coatings produced in Ar (a) and Ar/H_2 (b) plasmas highlighting the increase in melted material visible with the addition of hydrogen in the plasma.

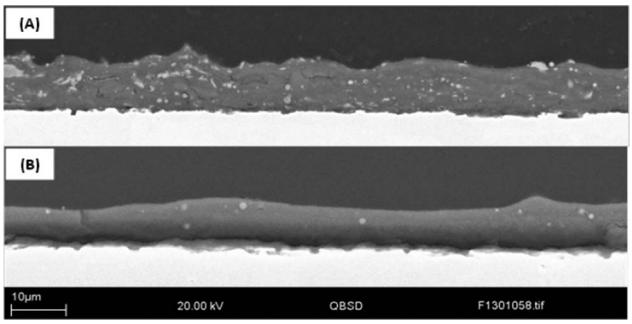

Fig. 10 The cross sections of SPS titania coatings produced in an Ar/H_2 plasma (a) and Ar plasma (b), respectively. Some damage was visible at the substrate coating interfaces. This damage can be said to have occurred during sectioning or metallographic grinding/polishing as there is no mounting epoxy in the void. Had the damage occurred during spraying, this void would be filled due to the use of vacuum impregnation during epoxy encapsulation before sample sectioning and mounting.

using Ar/H_2 plasma containing more melted areas than those from the Ar plasma (Fig. 10). Melted agglomerates were evenly distributed throughout the Ar/H_2 coatings with many appearing as oblongs, demonstrating their distortion on collision with the substrate.

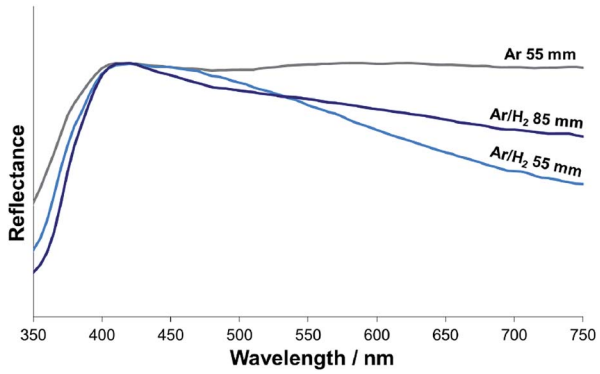

Fig. 11 UV-Vis spectra of coatings produced in the two plasma conditions, from the 12 nm feedstock at the two ends of the spray distance range.

3.7. UV-Vis absorption

All coatings had a band gap in the range of *ca.* 3.0–3.2 eV, typical of titania coatings (anatase 3.2 eV, rutile 3.0 eV), with no trend discernable with regards to spray conditions.

Coatings produced in the Ar/H_2 plasma demonstrated visible light absorbance with a significant decrease in reflectance at wavelengths >500 nm (Fig. 11). This is in agreement with visual observations of these coatings which appear blue in colour (Fig. 3). Absorbance in this range is due to the creation of Ti^{3+} within the coating as a result of reduction by the hydrogen containing plasma. This absorbance increases with decreasing stand-off distance, which is also in agreement with visual inspection of the coatings. This trend is attributed to re-oxidation of inflight particles at greater stand-off distances.

Coatings produced in the Ar plasma showed no significant absorbance in the visible range, as is typical for pristine titania (Fig. 11).

3.8. Photoactivity

Photoelectrochemical hydrogen production testing was performed using a sacrificial system to determine the photoactivity of the coatings. In this sacrificial test, hydrogen is collected from the photochemical breakdown of ethanol by the coatings.[32] This test is appropriate as it reflects similar circumstances to those in which a water purifying device may work, removing organic pollutants from water (ethanol in this scenario). This test also seemed appropriate for determining the performance of the coating in a photolysis device due to the production of hydrogen which can be measured quantitatively.

All coatings were robust and survived photocatalytic testing without significant damage. However, the substrates later corroded. This is thought to be due to the use of an etchant to structure the surface prior to spraying. Hence, this method of surface preparation would not be recommended in future.

The photocatalytic results (Fig. 12) showed that there is an initiation period where hydrogen production was slow due to

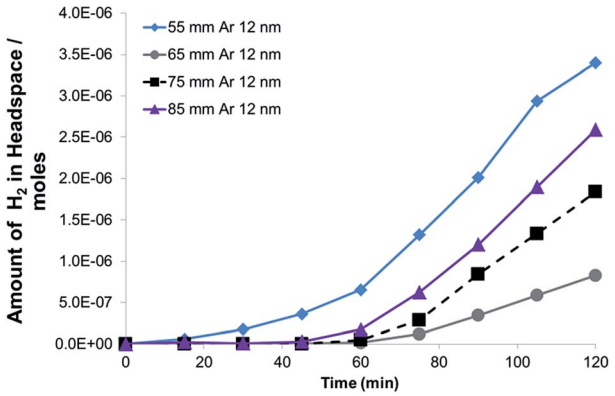

Fig. 12 The rate of hydrogen production from four SPS titania coatings in a sacrificial solution under UV irradiance.

the time taken for the surface to become saturated. This time period is also associated with saturation of the solution with hydrogen gas before it could fill the head space in the beaker.

Results show that all of the coatings produced were photoactive, though to differing degrees. A trend was observed in hydrogen production as a function of phase composition for the coatings produced using Ar/H_2 plasma (Fig. 13). The hydrogen production rate appeared to largely increase with increasing rutile content. This agrees with the theory of a synergistic relationship existing between anatase and rutile phases in close contact (alignment of bandgaps to facilitate effective photoexcited electron and hole pair vectorial charge separation). However, the greatest production rate observed, 99 mL m^{-2} h^{-1}, was measured for a near completely anatase phase coating. This is despite the widely accepted correlation of phase content with activity particularly with reference to the often quoted *ca.* 80% anatase optimum.[36] It should however be said that the role of other factors, specifically those relative to the surface, have recently also been highlighted as significant in affecting activity of titania coatings.[45] These factors include surface area (and roughness), degree of surface hydroxylation and the affinity of the surface for the relevant adsorbates.[46] It would seem that the

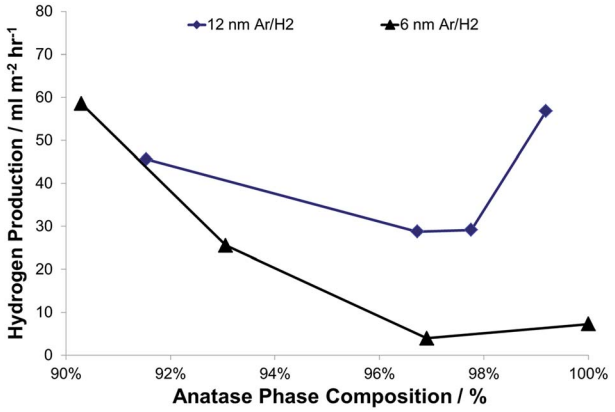

Fig. 13 The trend of hydrogen production *vs.* anatase phase content for the coatings produced using the Ar/H_2 plasma.

lack of a true trend in activity with anatase content, when considering all results, in this case may be due to a convolution of these factors. It is also possible that the presence of reduced species in the coatings produced using Ar/H_2 plasma (as seen by the sample colouration Fig. 3 and UV-Vis spectroscopy Fig. 11), resulted in a decreased activity by acting as recombination centres.[47] This could be the dominating effect such that rutile content may still have a positive influence on photoactivity. This may also explain the increase in photoactivity (slight for the 6 nm coatings and more significant for the 12 nm coatings) at the greatest stand-off distance for the coatings produced in the Ar/H_2 plasmas. A visible decrease in Ti^{3+} concentration can be observed through coating colour change (Fig. 3) as well as by UV-Vis spectroscopy (Fig. 11), with increasing stand-off distance, which may cause decreased recombination and an increase in photoactivity. This presents a challenge of inducing a phase change in the titania through the increase in temperature without the generation of reduced titania species or else having to introduce a subsequent reoxidizing step. It is possible that the absorbance of visible light which results from the creation of Ti^{3+} may yield enhanced photoactivity. However, testing in this instance was carried out under UV exposure and further research would be required to determine the role of Ti^{3+} in coating photoactivity.

Coatings composed of the 12 nm crystals were observed to be largely more active than those of the 6 nm coatings produced in corresponding conditions. This is attributed to a decreased rate of surface recombination occurring in the larger crystals.

To determine the activity of coatings produced here relative to other materials, the coatings can be compared with work on compressed discs of P25 (a commercial photocatalytic material composed of anatase and rutile titania) published by Elouali *et al.* where activity was determined by the same hydrogen evolution test.[33] In that report, P25 was compressed into discs and heat treated at varying temperatures to give hydrogen production rates of *ca.* 0.69–0.85 mol h^{-1} g^{-1} m^{-2} depending on the temperature at which the material was annealed. These results are comparable to the activities reported here for coatings produced by SPS where the most active coatings had a hydrogen production rate of 0.69 mol h^{-1} g^{-1} m^{-2}. This is despite the fact that in the case of the compressed discs of P25 the platinum and titania are in immediate contact, an arrangement that allows rapid electron transport from the titania to the platinum, desirable for maximum photoactivity. In the SPS coatings the steel substrate acts as a barrier increasing resistance in the system and lowering photoactivity. Compressed discs of P25 cannot be used as photo-catalytically active component in devices such as water purifiers due to their poor structural integrity. Results can also be compared with rutile CVD coatings produced by Hyett *et al.*[34] CVD titania coating produced in said paper where found to have hydrogen production rates of 0.01–0.22 μmol h^{-1} cm^{-2} depending on coating thickness. SPS coatings produced herein have been shown to have hydrogen production rates of up to 0.44 μmol h^{-1} cm^{-2}, twice that of the maximum reported for the CVD coating. Samples in both instances were produced on stainless steel, however CVD coatings were deposited on steel of 0.1 mm

thickness as oppose to the 0.5 mm thickness used for SPS samples. This would likely artificially raise the CVD coating H_2 production rates relative to SPS coatings due to a decreased distance for the electrons to travel.

4. Conclusions

Titania coatings were produced by suspension plasma spray of *ca.* 5 wt% CHFS water-based titania suspensions (*ca.* 6 and 12 nm) onto 304 stainless steel substrates. Phase composition of these coatings varied from 90–100% anatase, with only coatings produced from Ar/H_2 plasma showing any significant phase transformation. Coatings produced in Ar plasma were almost entirely unmelted in structure, being composed of densely packed crystallites. Samples produced in the Ar/H_2 plasma had a bimodal structure of dominant granular zones interrupted by melted and partially melted agglomerates impacted on the surface. These deformed, resolidified areas correlate with the minor percentage of rutile phase detected by XRD (confirmed using micro-Raman spectroscopy). Coatings produced in the Ar/H_2 plasma were showed to absorb light in the visible spectrum due to the presence of Ti^{3+}. All coatings produced herein were photoactive, with no conclusive correlation observed between activity and phase composition. The most active coating had a hydrogen production rate comparable to that of bulk P25 pressed discs and two times greater than titania CVD coatings reported for this test. The use of feedstocks produced by CHFS provided effective suspensions for the process and thus few blockages occurred during spraying. The stability of the suspensions was adequate, but should be improved in future *via* the use surface agents in the CHFS synthesis to induce surface charge stabilisation or steric stabilisation. The authors have developed citric acid coated TiO_2 that forms very stable suspensions in water; this work will be reported elsewhere. CHFS is an environmentally friendly process for producing a range of feedstocks suitable for suspension spray. The potential for co-location of CHFS with the suspension spraying processes provides an opportunity to develop a 'molecules to coating' technology.

Acknowledgements

The authors would like to thank Deepa Jose and David Hazafy of Queens University Belfast for their discussions of photocatalysis. Frank Nolan, Sheila Stevens and Simon Condie of TWI are thanked for their contributions in sample preparation, analysis and photography, respectively. Penny Carmichael, Neel Makwana, Dan Brett, Eric Fraga, Krisztian Ronaszegi, Steve Firth and Martin Vickers of UCL, Debbie Hammond of Tata Steel, Xiaoling Zhang and Kevin Cooke of MIBA (Teer Coatings Ltd) and Alan Smith of TSB are also thanked for their deliberations during the work. This research was partially funded by the UK's Technology Strategy Board (TSB) and the Engineering and Physical Sciences Research Council (EPSRC) under Project 100898 "Nanocrystalline Water Splitting Photodiodes II; Device Engineering, Integration & Scale-up". The associated ESPRC EngDoc sponsorship for B Robinson is 1st co-funded by TWI under UCL's Industrial Doctorate Centre in Molecular Modelling & Materials Science.

Notes and references

1 D. T. Tran and R. Salmon, *Australas. J. Dermatol.*, 2011, **52**, 1–6.
2 G. Plesch, M. Vargova, U. F. Vogt, M. Gorbar and K. Jesenak, *Mater. Res. Bull.*, 2012, **47**, 1680–1686.
3 M. El-Roz, M. Kus, P. Cool and F. Thibault-Starzyk, *J. Phys. Chem. C*, 2012, **116**, 13252–13263.
4 A. Subramanian and H. W. Wang, *Appl. Surf. Sci.*, 2012, **258**, 7833–7838.
5 B. D. Alexander, P. J. Kulesza, L. Rutkowska, R. Solarska and J. Augustynski, *J. Mater. Chem.*, 2008, **18**, 2298–2303.
6 S. Banerjee, J. Gopal, P. Muraleedharan, A. K. Tyagi and B. Rai, *Curr. Sci.*, 2006, **90**, 1378–1383.
7 J. Yan and F. Zhou, *J. Mater. Chem.*, 2011, **21**, 9406–9418.
8 Z. Zhang, J. Goodall, D. J. Morgan, S. Brown, R. J. Clark, J. C. Knowles, N. J. Mordan, J. R. Evans, A. F. Carley and M. Bowker, *J. Eur. Ceram. Soc.*, 2009, **29**, 2343–2353.
9 C. W. Dunnill, A. Kafizas and I. P. Parkin, *Chem. Vap. Deposition*, 2012, **18**, 89–101.
10 T. Yazawa, F. Machida, N. Kubo and T. Jin, *Ceram. Int.*, 2009, **35**, 3321–3325.
11 L. Ma, M. Liu, T. Y. Peng, K. Fan, L. L. Lu and K. Dai, *Mater. Chem. Phys.*, 2009, **118**, 477–483.
12 S. Ito, P. Chen, P. Comte, M. K. Nazeeruddin, P. Liska, P. Pechy and M. Gratzel, *Prog. Photovoltaics*, 2007, **15**, 603–612.
13 A. Fernandez, G. Lassaletta, V. M. Jimenez, A. Justo, A. R. Gonzalez-Elipe, J.-M. Herrmann, H. Tahiri and Y. Ait-Ichou, *Appl. Catal., B*, 1995, **7**, 49–63.
14 F. L. Toma, G. Bertrand, D. Klein, C. Meunier and S. Begin, *J. Nanomater.*, 2008, 384171.
15 N. George, M. Mahon and A. McDonald, *J. Therm. Spray Technol.*, 2010, **19**, 1042–1053.
16 E. M. Cotler, D. Y. Chen and R. J. Molz, *J. Therm. Spray Technol.*, 2011, **20**, 967–973.
17 R. Jaworski, L. Pawlowski, F. Roudet, S. Kozerski and A. Le Maguer, *J. Therm. Spray Technol.*, 2008, **17**, 73–81.
18 F. L. Toma, L. M. Berger, D. Jacquet, D. Wicky, I. Villaluenga, Y. R. de Miguel and J. S. Lindelov, *Surf. Coat. Technol.*, 2009, **203**, 2150–2156.
19 F. L. Toma, L. M. Berger, C. C. Stahr, T. Naumann and S. Langner, *J. Therm. Spray Technol.*, 2010, **19**, 262–274.
20 F. L. Toma, D. Sokolov, G. Bertrand, D. Klein, C. Coddet and C. Meunier, *J. Therm. Spray Technol.*, 2006, **15**, 576–581.
21 F. L. Toma, G. Bertrand, S. O. Chwa, C. Meunier, D. Klein and C. Coddet, *Surf. Coat. Technol.*, 2006, **200**, 5855–5862.
22 S. Kozerski, F. L. Toma, L. Pawlowski, B. Leupolt, L. Latka and L. M. Berger, *Surf. Coat. Technol.*, 2010, **205**, 980–986.
23 F. L. Toma, G. Bertrand, D. Klein, C. Coddet and C. Meunier, *J. Therm. Spray Technol.*, 2006, **15**, 587–592.
24 F. L. Toma, G. Bertrand, D. Klein, C. Meunier and S. Begin, *J. Nanomater.*, 2008, 8.

25 G. Bolelli, V. Cannillo, R. Gadow, A. Killinger, L. Lusvarghi and J. Rauch, *Surf. Coat. Technol.*, 2009, **203**, 1722–1732.
26 K. Eufinger, D. Poelman, H. Poelman, R. De Gryse and G. Marin, *Thin Solid Films*, 2008, **37**, 2.
27 C. J. Tighe, R. I. Gruar, C. Y. Ma, T. Mahmud, X. Z. Wang and J. A. Darr, *J. Supercrit. Fluids*, 2012, **62**, 165–172.
28 C. J. Tighe, R. Q. Cabrera, R. I. Gruar and J. A. Darr, *Ind. Eng. Chem. Res.*, 2013, **52**, 5522–5528.
29 R. Gruar, C. Tighe and J. Darr, *Ind. Eng. Chem. Res.*, 2013, **52**, 5270–5281.
30 Z. Zhang, S. Brown, J. Goodall, X. Weng, K. Thompson, K. Gong, S. Kellici, R. J. Clark, J. R. Evans and J. A. Darr, *J. Alloys Compd.*, 2009, **476**, 451–456.
31 Z. Zhang, X. Weng, K. Gong and J. Darr, in *Technical Proceedings of the 2008 NSTI Nanotechnology Conference and Trade Show*, NSTI-Nanotech, Nanotechnology, 2008.
32 P. Carmichael, D. Hazafy, D. S. Bhachu, A. Mills, J. A. Darr and I. P. Parkin, *Phys. Chem. Chem. Phys.*, 2013, **15**, 16788–16794.
33 S. Elouali, A. Mills, I. P. Parkin, E. Bailey, P. F. McMillan and J. A. Darr, *J. Photochem. Photobiol., A*, 2010, **216**, 110–114.
34 G. Hyett, J. A. Darr, A. Mills and I. P. Parkin, *Chem. Vap. Deposition*, 2010, **16**, 301–304.
35 P. I. Gouma and M. J. Mills, *J. Am. Ceram. Soc.*, 2001, **84**, 619–622.
36 M. Kang, D. H. Choi and S. J. Choung, *J. Ind. Eng. Chem.*, 2005, **11**, 240–247.
37 Y. K. Kho, A. Iwase, W. Y. Teoh, L. Madler, A. Kudo and R. Amal, *J. Phys. Chem. C*, 2010, **114**, 2821–2829.
38 D. Scanlon, C. Dunnill, J. Buckeridge, S. Shevlin, A. Logsdail, S. Woodley, T. W. Keal, M. Powell, R. Palgrave, I. Parkin, G. Watson, P. Sherwood, A. Walsh and A. Sokol, *Nat. Mater.*, 2013, **12**, 798–801.
39 E. Bemporad, G. Bolelli, V. Cannillo, D. De Felicis, R. Gadow, A. Killinger, L. Lusvarghi, J. Rauch and M. Sebastiani, *Surf. Coat. Technol.*, 2010, **204**, 3902–3910.
40 G. Mauer, A. Guignard, R. Vassen and R. Vaßen, *Surf. Coat. Technol.*, 2013, **220**, 40–43.
41 RRUFF, Anatase R120013, http://rruff.info/repository/sample_child_record_raman/by_minerals/Anatase__R120013__Raman__780__0__unoriented__Raman_Data_Processed__36398.txt, Accessed 26/03/13.
42 RRUFF, Rutile R060493, http://rruff.info/repository/sample_child_record_raman/by_minerals/Rutile__R060493__Raman__532__0__unoriented__Raman_Data_Processed__10258.txt, Accessed 26/03/13.
43 C. Almquist and P. Biswas, *J. Catal.*, 2002, **212**, 145–156.
44 K. Y. Jung, S. Bin Park and S. K. Ihm, *Appl. Catal., A*, 2002, **224**, 229–237.
45 E. Bannier, G. Darut, E. Sanchez, A. Denoirjean, M. C. Bordes, M. D. Salvador, E. Rayon and H. Ageorges, *Surf. Coat. Technol.*, 2011, **206**, 378–386.
46 G. H. Wang, L. Xu, J. Zhang, T. T. Yin and D. Y. Han, *Int. J. Photoenergy*, 2012, 9.
47 L.-B. Xiong, J.-L. Li, B. Yang and Y. Yu, *J. Nanomater.*, 2012, **2012**, 1–13.